LLNL-JRNL-665451

LAWRENCE
LIVERMORE
NATIONAL
LABORATORY

The effect of nearly steady shock waves in ramp compression experiments

D. E. Fratanduono, R. F. Smith, D. G. Braun, J. R. Patterson, R. G. Kraus, T. S. Perry, A. Arsenlis, G. W. Collins, J. H. Eggert

December 15, 2014

Journal of Applied Physics

Disclaimer

The effect of nearly steady shock waves in ramp compression experiments

D. E. Fratanduono, R. F. Smith, D. G. Braun, J. R. Patterson, R. G. Kraus, T. S. Perry, A. Arsenlis, G. W. Collins, J. H. Eggert
Lawrence Livermore National Laboratory
(Dated: June 1, 2015)

The iterative Lagrangian analysis (ILA) applied to free-surface velocity measurements of ramp-compressed samples is an established technique to determine the stress-density response of materials up to 50 Mbar pressures. In this work, we examine the accuracy of the ILA of ramp compression profiles with multiple shock waves present through the analysis of simulated compression profiles. The results presented indicate that ramp-compression data with weak shock waves can be analyzed using the ILA to quantitatively measure the absolute stress and density along the compression path.

I. INTRODUCTION

Knowledge of a material's equation of state (EOS) under conditions of extreme pressure, temperature and density is important to a variety of fields (e.g. condensed-matter physics, geophysics, and inertial confinement fusion). For instance, recent density-functional-theory calculations predict complex high-pressure (>10 Mbar) and low-temperature (<1 eV) crystal structures[1–3] that contradict the early Wigner and Seitz[4] description of matter at high pressure.[5] Exploration of these newly proposed structures at low temperature and high pressures are now accessible through ramp compression and can be diagnosed through dynamic x-ray diffraction.[6] Further, there is significant interest in the geophysical community to understand the interior structure of terrestrial planets within our own solar system,[7] as well as the interior structures of observed super-Earths.[8,9] An accurate EOS, at high pressure and low temperature is needed to understand the thermal evolution of these extra-solar planets.[10] Due to the interest in high-pressure EOS, the National Ignition Facility (NIF)[11] and the Z-Machine[12] are pushing the limits of EOS measurements into the 10's Mbar regime through both shock and ramp compression.[13–16]

Single shock measurements produce high-pressure and high-temperature states, often melting the sample under study. In contrast, recently developed high-pressure ramp-wave loading experiments produce less dissipative-heating, thus enabling access to higher-compression and lower-temperature states.[15,17] In ramp-wave loading experiments, the analysis of free-surface velocity histories from multiple thickness samples can yield continuous measurements of Lagrangian sound speed (C_L), longitudinal stress (σ_{xx}), density (ρ), and particle velocity (U_p). This is achieved through an iterative Lagrangian analysis (ILA) which corrects for wave interactions at the sample's free surface.[18,19] Ideally, shockless ramp-wave loading EOS measurements describe the material isentrope but deviations from this path may result from material strength, rate-dependent deformation effects and other dissipative processes.[20]

Gas-gun[21] experiments have employed reverberating shocks to achieve high-density states close to the isentrope.[22–25] Specifically, Nellis[25] showed that for 10-fold compressed liquid hydrogen, 9 shock reverberations closely follows the principal isentrope of hydrogen to 180 GPa in stress-density space. This approximation derives from the fact that a ramp wave can be approximated by an infinite number of weak shocks.[26] In this work, we look to understand the implications of weak shocks in the ILA.

Using hydrocode simulations, we examine the effect of intermediate shock waves on the pressure-density path. Today's laser-based ramp-compression experiments have random uncertainties of the order of 5% in stress and compression for a single experiment[15,20,27] which sets a practical definition of a weak shock (e.g. a shock that imposes less than a 1% deviation in compression from the isentrope such that the systematic uncertainty is small compared to the random uncertainties). We show that the existence of nearly-steady weak shock waves in ramp-wave loading EOS experiments do not significantly perturb the stress-density path obtained by the ILA when compared to the true stress-density path of the sample. We also examine the validity of the ILA when shocks are present in determining the stress-density. These findings relax the design criteria on ramp-wave loading EOS experiments and help to extend this technique to higher-pressure regimes.

II. THEORY

The ILA was first proposed by Maw and Rothman[18,19,28] to extract ramp-compression paths in the stress-density plane on data without shock waves present. The technique consists of measuring the free-surface velocity history of a multi-step target where velocity-time data are used as input into a characteristics algorithm. The analysis corrects for the wave interactions between the incoming compression waves (forward characteristics) and the reflected decompression waves (backwards characteristic) in order to map the free-surface velocity to the *in situ* particle velocity. The algorithm back propagates the free-surface measurements to the loading surface using an assumed $C_L(U_p)$ for the material under study. Once the resulted stress at the loading surface is determined for each step, the characteristics are forward propagated where the free-surface boundary condition has been changed to an *in situ* condition. The corrected *in situ* particle-velocity histories at positions equal to the free-surface locations are determined for each sample thickness. $C_L(U_p)$ is fit to the corrected U_p histories and the analysis is iterated until $C_L(U_p)$ converges.

The ILA is based on the assumption that isentropic compression information travels along hydrodynamic characteristics that propagate at the local sound speed (simple wave approximation) and that the particle velocity and pressure perturbations travel at the same speed. In the one-dimensional Lagrangian frame of reference, the mass and momentum conservation equations can be combined as

$$\Big(\frac{\partial C_L}{\partial t} \pm C_L\frac{\partial U_p}{\partial h}\Big) \pm \frac{1}{\rho_0 C_L}\Big(\frac{\partial P}{\partial t} \pm C_L\frac{\partial P}{\partial h}\Big) = 0, \qquad (1)$$

where P is the hydrostatic pressure, ρ_0 is the ambient density, t is time, h is the Lagrangian position and C_L is the Lagrangian sound speed defined as

$$C_L^2 = \frac{\rho^2}{\rho_0^2}\frac{\partial P}{\partial \rho}\Big|_S, \qquad (2)$$

where S is entropy. The equations for the characteristics become

$$\frac{dh}{dt}\Big|_{\pm} = \pm C_L, \qquad (3)$$

for the forward $(+)$ and backwards $(-)$ propagating characteristics. The Riemann invariants are

$$dU_p \pm \frac{dP}{\rho_0 C_L} = 0 \text{ along } \pm C_L, \qquad (4)$$

and

$$dU_p \pm \rho_0 C_L \frac{d\rho}{\rho^2} = 0 \text{ along } \pm C_L. \qquad (5)$$

The compression and pressure along the isentrope take the form

$$\frac{1}{\rho_1} - \frac{1}{\rho_2} = \int_{U_{p1}}^{U_{p2}} \frac{dU_p}{\rho_0 C_L}, \qquad (6)$$

and

$$P_2 - P_1 = \int_{U_{p1}}^{U_{p2}} \rho_0 C_L dU_p, \qquad (7)$$

respectively. Since $dS = 0$, the energy (E) is defined as

$$E_2 - E_1 = \int_{\rho_1}^{\rho_2} P\frac{d\rho}{\rho^2}, \qquad (8)$$

where the integrals span compression from an initial state '1' to a final state '2'. In isentropic ramp compression experiments, the density, hydrostatic pressure and energy are determined from continuous measurements of the particle velocity and sound speed.

It is important to note that the variables ρ_1, P_1 and E_1 represent state variables from which ramp compression is initiated (either from a shocked state or ambient conditions). In this work, shock and ramp compression profiles are mixed and the ILA occurs in the Lagrangian frame of reference. It is important to discern between ρ_0 and ρ_1. Subscript 0 denotes values at ambient conditions, while subscripts 1 may represent the values at an initially compressed state.

In contrast, the Rankine-Hugoniot equations that describe shock compression are discrete: they relate an initial state to an end state linked through a non-isentropic shock front. In the Lagrangian frame of reference, the Rankine-Hugoniot equations for conservation of mass, momentum and energy are

$$\frac{1}{\rho_1} - \frac{1}{\rho_2} = \frac{U_{p2} - U_{p1}}{\rho_0 D_L}, \qquad (9)$$

$$P_2 - P_1 = \rho_0 D_L (U_{p2} - U_{p1}), \qquad (10)$$

and

$$E_2 - E_1 = \frac{(P_2 + P_1)}{2}\Big(\frac{\rho_2 - \rho_1}{\rho_2 \rho_1}\Big), \qquad (11)$$

where D_L is the shock velocity in the Lagrangian frame and subscripts "1" and "2" refer to the pre- and post-shock conditions, respectively.

An important consideration to note is the similarity between the isentropic equations (6)-(8) and the Rankine-Hugoniot equations (9)-(11). One may show that the difference in pressure, particle velocity and density between a weak shock and ramp compression differ to third order.[26,29,30] The entropy associated with a given shock magnitude is

$$S_2 - S_1 = \frac{1}{6\rho_1^2 T_1 C_{L,1}^3}\frac{\partial C_L}{\partial P}\Big|_{S_1}(P_2 - P_1)^3. \qquad (12)$$

Since ρ_1, T_1 and $C_{L,1}$ increase while $\frac{\partial C_L}{\partial P}\Big|_{S_1}$ decreases with increasing P_1 the entropy contributed by a shock decreases with P. As the initial pressure increases, the deviation from the isentrope for a shock of constant magnitude is decreased.

For a weak shock wave, the Lagrangian shock velocity can be approximated by the average of the Lagrangian sound speed ahead and behind the shock front.[30] Consider the Rankine-Hugoniot conservation of mass equation in Lagrangian coordinates (equation 9),

$$D_L = \frac{dh}{dt} = \frac{\rho_2\rho_1}{\rho_0}\frac{U_{p2} - U_{p1}}{\rho_2 - \rho_1}. \qquad (13)$$

By Taylor expanding $U_p(\rho)$ about the average density state ($\overline{\rho} = (\rho_1 + \rho_2)/2$) and utilizing equation 2, one may show that to second order in compression

$$D_L \approx \overline{C}_L - \frac{(\Delta\rho)^2}{\rho_0}\Big(\frac{dU_p}{d\rho} - \frac{\overline{\rho}^2}{6}\frac{d^3U_p}{d\rho^3}\Big), \qquad (14)$$

where $\overline{C_L} = \frac{C_{L,2}+C_{L,1}}{2}$ and $\Delta\rho = \rho_2 - \rho_1$. Equation 14 indicates that weak shocks propagate at the average sound speed to first order in density.

In ramp compression experiments, the assumption of constant entropy ($\Delta S = 0$) is often violated not only by the potential presence of weak shocks due to non-ideal loading rate, but also by the plasticity of the material. However, for uniaxial compression, the measured sound speed of the system can

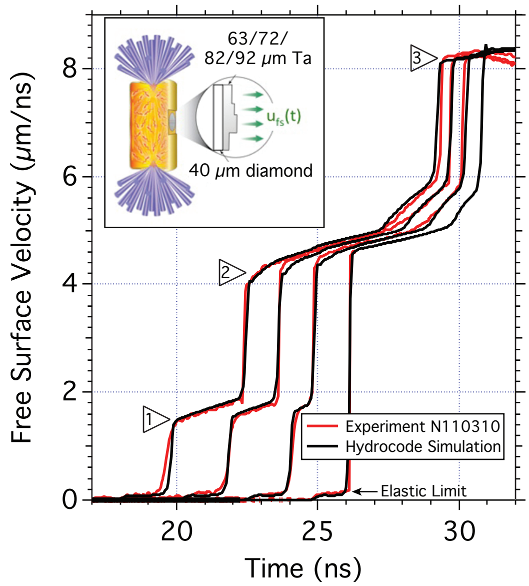

FIG. 1: Experimental data from NIF shot N110310 used as a reference experiment in this work. Three shock waves are observed as fringe discontinuities and are enumerated. The extracted VISAR free-surface velocities are shown in red. LASNEX simulated free-surface velocity using Sesame table 3520 are shown in black. Inset shows the target design.

still be related to the stress-density. Using mass and momentum conservation laws, one may show that the propagation speed of a longitudinal stress (σ_{xx}) perturbation is defined as the *total* derivative of stress with respect to density,

$$C_L^2 = \frac{\rho^2}{\rho_0^2}\frac{d\sigma_{xx}}{d\rho}. \tag{15}$$

No assumptions need be made regarding reversibility or the process being isentropic; the only assumption is that the perturbations are small. Ramp-compression experiments with weak shocks and strength measure the propagation speed (not to be confused with the isentropic sound speed) within the sample, which can be integrated to give the stress-density using equation (15).

A series of experiments have been performed at the National Ignition Facility[11] (NIF) to measure the ramp compressed stress-density path of tantalum. In some of these experiments, a series of weak shocks waves were observed in the compression profile due to a non-ideal loading rate. Since the effect of weak shock waves in ramp compression experiments can be small, it may be possible to use the ILA to analyze Ta ramp compression experiments with weak shock waves present. We test this hypothesis on a post-shot hydro simulation of a NIF reference experiment using the ILA.

III. REFERENCE EXPERIMENT

To examine the effect of weak shock waves on ramp compression experiments and the ILA technique at relevant conditions, we simulated the free-surface velocities observed in a reference experiment (N110310) that was performed on the NIF. Please note that the experimental results (the measured Lagrangian sound speed, particle velocity, stress, and density) from that NIF experiment are not presented herein. In our simulations of the reference experiment, Ta was compressed by a combination of shock and shock-less compression waves and the stress-density path was extracted to a peak longitudinal stress of 6 Mbar. In the reference experiment, the sample consisted of a 40 μm thick diamond ablator and four Ta samples with thicknesses of 63 / 72 / 82 / 92 μm (Figure 1 inset). The sample package was placed on the side of a gold hohlraum[31] that was illuminated by 176 beams of the NIF with a combined energy of 162 kJ in a 27 ns temporally ramped pulse.[7] This generated a spatially-uniform distribution of thermal x rays that ablated the diamond and produced a spatially-uniform compression wave. The arrival of the compression wave at the rear surface of the Ta target produced a free-surface velocity history ($U_{fs}(t)$) that was recorded with a line-imaging velocity interferometer (VISAR)[32]. The free-surface velocity profiles measured using VISAR are shown in Figure 1 as red lines. The data indicates that the ramp-compression profile is characterized as a sequence of shocks and ramps. The first shock wave corresponds to the arrival of the diamond Hugoniot elastic limit. The subsequent shocks are modeled in our simulations by a time dependent pressure-drive determined to best fit the experimental free-surface velocities; the resulting simulated velocities are shown as black lines in Figure 1.

Due to the nonlinear stress-density relationship, and the incumbent difficulty in obtaining truly shockless compression to multi-Mbar stress states, intended ramp-compression experiments often have shocks in the free-surface velocity. This free-surface velocity information can still be used to constrain the material response, albeit not as accurately as when true shockless compression is obtained. Since a ramp compression path can be characterized by a series of shock and ramps, this experiment was simulated to illustrate the effects of seemingly strong shock waves on the stress-density path and the ILA, where we define a weak shock to be any shock that causes a small effect on the stress-density path.

IV. HYDROCODE SIMULATIONS

The experimental results shown in Figure 1 are simulated using the LASNEX[33] hydrocode. The LASNEX simulations are conducted in a 1D geometry, neglecting the 2D effects of lateral release from the drive surface and the step edges,[34] with zone sizes of 0.25 μm and examined using both a soft (Sesame table 3520) and stiff (LEOS table 739) EOS and similar conclusions are drawn from the analysis of both simulations.[35,36] Sesame 3520 uses a Thomas-Fermi-Dirac thermal electronic model with Kohn-Sham potential. The cold curve was generated from a linear fit to the existing shock data reproducing the Hugoniot data to within 0.4% over the experimental range. The tantalum LEOS 739 equation of state is a tabular EOS model in the LLNL LEOS data library constructed by D. A. Young (2001, unpublished). It is based on

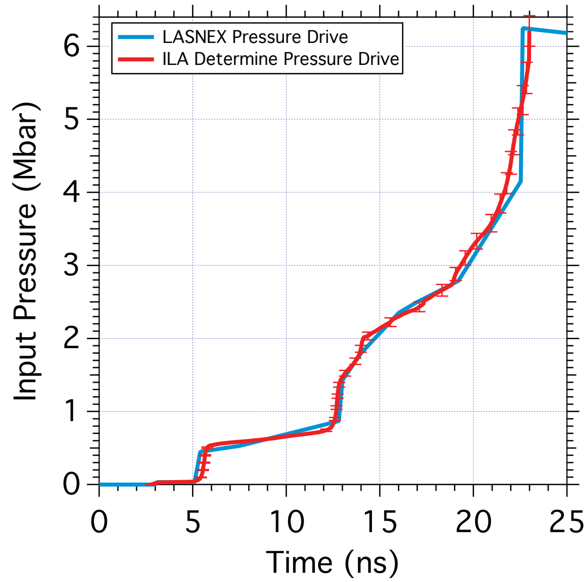

FIG. 2: The LASNEX input drive pressure is shown in blue. The ILA determined input pressure drive using the LASNEX simulated free-surface velocity profiles is shown in red.

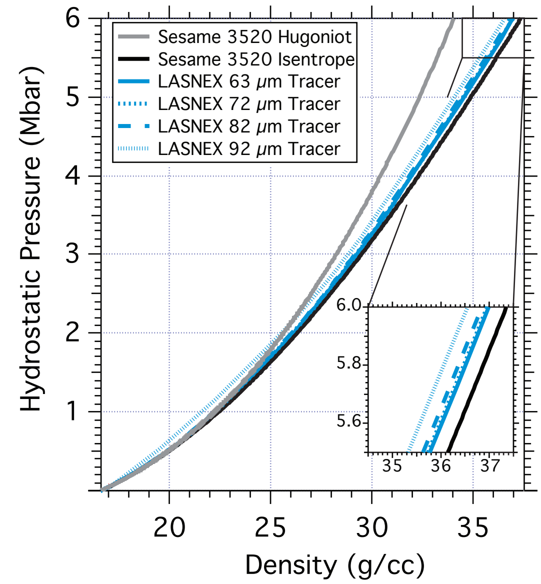

FIG. 3: The LASNEX simulated hydrostatic pressure vs. density using Sesame table 3520. The hydrostatic pressure for each of the LASNEX tracer particles (blue lines) is compared to the principal Hugoniot (grey) and isentrope (black).

a QEOS-like model[36] with the addition of cold-curve break-points.[37] A Steinberg-Guinan strength model is used in these simulations to reproduce the initial elastic wave (the increase in free-surface velocity from 0 to 0.1 km/s in each step). A suitable input pressure drive at the diamond/tantalum sample for each table is determined which reproduces the experimental features observed in each step. The input LASNEX pressure drive used for the Sesame 3520 simulation is shown in Figure 2.

The hydrocode simulations using Sesame table 3520 are shown in Figure 1 as black lines. After determining the input pressure drive that best reproduces the experimental results, another hydrocode simulation was conducted with an semi-infinite thick sample to determine the unperturbed *in-situ* thermodynamic variables at the Lagrangian positions consistent with each step height. *In-situ* tracer particles were placed at 63 / 72 / 82 / 92 μm from the loading surface. In the following subsections, the hydrocode simulations are examined in detail. In Subsection IV A, the hydrostatic pressure versus density is examined to estimate the deviation from the principal isentrope due to work and shock heating. In subsection IV B, the ILA results are compared to the LASNEX tracer particles to examine the validity of the ILA technique when weak shocks are present.

A. Hydrostatic Pressure

LASNEX simulations enable the isolation of non-hydrostatic contributions to the total stress which allows us to examine the hydrostatic pressure-density of each element during the compression history and to compare with the ideal hydrostatic isentrope associated with the EOS table. The LASNEX simulated pressure-density path is shown in Figure 3. The Hugoniot and isentrope from the Sesame table 3520 are shown as the grey and black curves, respectively. The pressure path calculated for each tracer particle is also shown. At peak compression, the three thinnest tracers are nearly consistent with one another (see Table I). The small differences are attributed to the fact that the shocks are growing with propagation distance through the sample. As the magnitude of the shock discontinuity is greater for the thicker steps, the resulting pressure-density path of the tracer particles is less compressible (stiffer) for the thicker steps as more heating occurs. All tracer particles are less compressible than the isentrope due to shock heating (increased levels of thermal pressure).

The LASNEX calculated temperature for each tracer particle at peak compression is shown in Table I. The LASNEX simulations indicate that due to the three shock waves, the temperature is greater than the isentrope by $\sim$ 3,100 K for the thinnest step. Since the shock waves are not steady, but grow with propagation distance, the thicker steps achieve higher-temperature states. For the thickest sample, the second shock has over taken the first. The LASNEX simulations find that the temperature of this step is $\sim$ 5,600 K hotter than the isentrope. Although three shock waves are present in the simulation, the temperature at maximum compression is much colder than the principal Hugoniot.

LASNEX simulations indicate that the pressure-density path of the tracer particles are systematically stiffer than the isentrope. By accounting for the initial shock state, the difference between the final state and the isentrope determined from the first shock state ($\sim$ 0.6 Mbar) is slightly reduced[27]

TABLE I: LASNEX simulations results for four different tracer particles compared to the principal Hugoniot, principal isentrope and the isentrope emanating from a state of 0.6 Mbar on the principal Hugoniot. All states are evaluated at a hydrostatic pressure of 6 Mbar.

	Density Deviation from Isentrope	Density g/cc	Temp. K	Entropy J/(g K)
Principal Hugoniot	8.83 %	34.05	24,000	0.836
Principal Isentrope	0 %	37.35	746	0.211
Isentrope from 0.60 Mbar shock state	0.29 %	37.24	1,489	0.309
63 μm tracer	0.96 %	36.99	3,850	0.453
72 μm tracer	1.04 %	36.96	4,130	0.465
82 μm tracer	1.26 %	36.88	4,860	0.492
92 μm tracer	2.14 %	36.55	6,350	0.537

as shown in Table I. This is an important consideration for ramp compression experiments that begin from a well-defined initial shock state, as they may be well constrained if the principle Hugoniot is known. These simulations illustrate that the pressure-density path is stiffer than the principle isentrope due to the heat added to the system by the shocks.

B. Iterative Lagrangian Analysis

The LASNEX-simulated free-surface velocity profiles shown in Figure 1 are used as input into the ILA[18,19] to determine the stress-density path and examine the validity of the method when nearly-steady shock waves are present. In this analysis, we *assume* that the waves are simple and apply no correction for the shocks or material strength. The ILA sound-speed versus particle velocity is shown as the red trace in Figure 4 and the ILA input pressure drive is shown in Figure 2 as the red line.

The *in-situ* Lagrangian sound speed is determined at each tracer and are shown as the dashed blue lines in Figure 4. The principal isentrope is shown in black and the sound speed determined using the ILA is shown in red. As shown in equation (7), the stress along the isentrope is proportional to the area below the isentrope in Figure 4(A) (grey shaded region). Equation (6) shows that the compression along the isentrope is related to the area below the isentrope in Figure 4(B) (grey shaded region).

The tracer particles in Figure 4 show a step-like feature in the $C_L - U_p$ path while the isentrope varies smoothly. These step features are indicative of the free-surface discontinuities shown in Figure 1(B) that correspond to the arrival of shock waves at the free surface. Further examination of these features indicate that they grow with tracer location indicating a degree of non-steadiness in the shocks. The inset in Figure 4 magnifies the region near the second shock wave in the simulation.

A simple Lagrangian analysis of the LASNEX *in situ* particle velocity traces corresponding to the 63 μm, 72 μm and 82 μm steps is shown in Figure 4 as the solid brown line. The

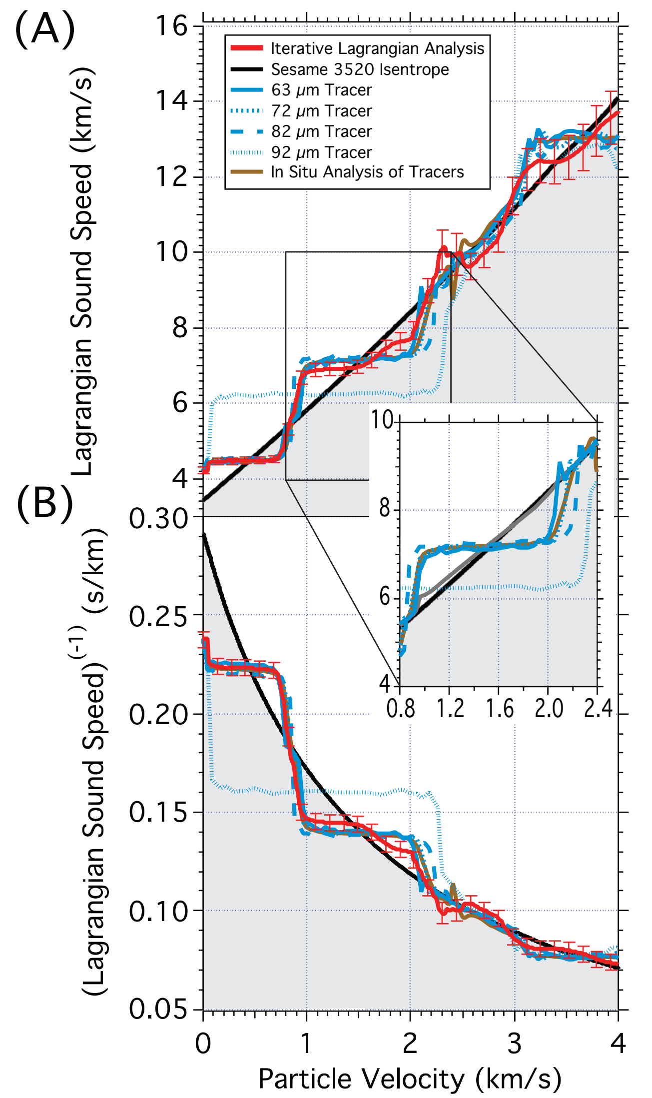

FIG. 4: The comparison of the Lagrangian sound speed determined from LASNEX *in situ* tracer particles (shown as blue dashed lines), the Lagrangian sound speed determined using the LASNEX simulated free-surface profiles and the ILA (shown in red) and *in-situ* analysis of the LASNEX tracer particles (shown in brown). The hydrocode simulations used Sesame table 3520 and the principal isentrope is shown in black. (A) The integrated area below the isentrope determines the stress (see equation 7). (B) The integrated area below the isentrope is *related* to the compression (see equation 6)

.

simple Lagrangian analysis tracks the 72 μm (the average of the threes steps) over nearly the entire $C_L - U_p$ plot below, except between 2.5 km/s and 3.0 km/s where a slightly higher sound speed is observed. Examination of the LASNEX simulations indicates that the higher sound speed is attributed to the coalescence of the first and second shock wave downrange of the tracers (recall that LASNEX simulates semi-infinite thick sample). Upon coalescence of the first and second shock wave, a counter-propagating characteristic is generated. The counter-propagating characteristic interacts with the 82 μm step at 2.3 km/s and the 63 μm step at 2.9 km/s. In the simple Lagrangian analysis, the counter-propagating wave is not accounted for and artificially increases the Lagrangian sound speed. It is important to note that this counter-propagating wave does not occur in the finite thickness samples, as the waves for the 63 μm, 72 μm and 82 μm steps arrive at the free surface before shock coalescence is observed. Figure 4 shows a disagreement between the simple Lagrangian analysis of the *in situ* particle velocity and the ILA results (show in red). Since the simple Lagrangian analysis is consistent with the *in situ* tracers, the disagreement with the ILA may be attributed to an error with the free-surface correction.

The stress-density path determined from the ILA of the LASNEX simulation is shown in Figure 5 in red (shock discontinuities are shown as dashed red Rayleigh lines and ramp compression paths are shown a solid red lines). Error bars in stress-density are plotted only at the shock-ramp intersections, but result from the propagation of uncertainties in the Lagrangian sound speed throughout the compression. The characteristic analysis determines the longitudinal stress, σ_{xx} in the sample since the LASNEX simulated free-surface velocities are influenced by the Ta strength. As a result, we are not able to compare the extracted profile with the corresponding isentrope, but instead with the longitudinal stress determined by tracer particles within the simulation. The propagated experimental uncertainties discussed in Section IV are shown. Comparison of the stress-density path determined using the ILA for the first three steps with those calculated for the tracer particles in the LASNEX simulations yields a difference of less than 0.7% (see Table II); a value small relative to the typical experimental uncertainty of about 3.5% shown by the error bars, indicating that the ILA is appropriate for this reference case. It is important to note that the fourth step, where the second shock has overtaken the first is significantly stiffer than the other steps and as a result only the three thinnest steps are used in the ILA.

The presence of shock waves in ramp-compression profiles leads to a roughly rectangular approximation of the $C_L - U_p$ relation. The $C_L - U_p$ data shows that the shock-step function follows a path that is initially above and then below the isentrope. Equation 14 indicates that weak shock waves in ramp compression data will manifest as step functions in the extracted Lagrangian sound speed versus particle velocity. These features are evident in both the Lagrangian sound speed determined in the LASNEX simulations and the ILA as shown in Figure 4. If we assume that for small discontinuities, the relation between the Lagrangian sound speed and particle velocity is linear ($C_L = a + bU_p$), one may show using equation 7 that the difference in the final stress state when comparing a weak shock to a ramp is third order in density. Thus, the stiffer stress-density path is mainly due to the decrease in density and the ILA results in a stiffer calculated response. This is easily observed in Figure 4 where the approximate area below and above the isentrope for the tracer particles are nearly equal in Figure 4A but not in Figure 4B.

TABLE II: LASNEX simulations and ILA evaluated at a longitudinal stress of 6 Mbar.

	Deviation from 63 μm tracer	Density g/cc
63 μm tracer	0 %	36.59
72 μm tracer	0.05 %	36.57
82 μm tracer	0.4 %	36.46
92 μm tracer	1.1 %	36.19
ILA	0.7 %	36.33

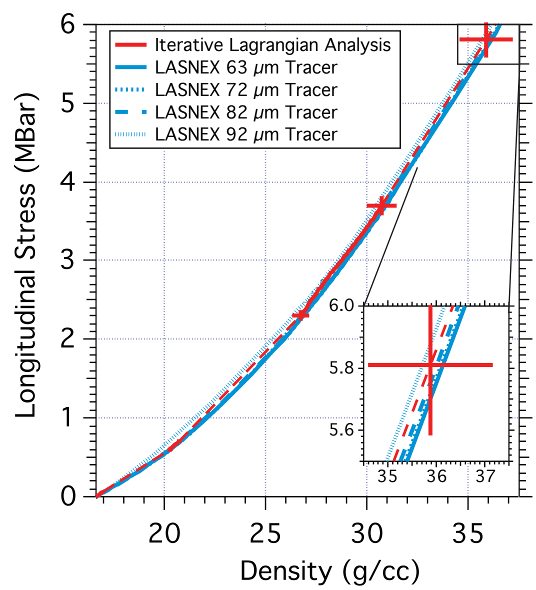

FIG. 5: The LASNEX simulated stress-density paths using Sesame table 3520. The stress-density path determined using the LASNEX free-surface velocity profiles and the ILA (shown in red). The three shock waves are indicated by their corresponding Rayleigh lines (shown as thin dashed red lines). Solid lines, with error bars, indicate regions that were ramped compressed. Error bars are plotted only at the intersections of shocked and ramp portions of the compression (and near peak compression), but result from error propagation throughout. The stress-density path of the ILA is compared to the stress observed by the four LASNEX tracer particles (blue lines).

V. CONCLUSIONS

Using LASNEX hydrocode simulations, we have shown that the presence of three shock waves in a ramp compression experiment produces a small deviation from the principal isentrope ($\sim$ 1.3% in density at peak pressure). The magnitude of intermediate shocks exceed 2 Mbar but results in small deviations from the isentrope in the pressure-density plane. Due to shock heating, the pressure-density path is systematically stiffer and represents an upper bound to the isentrope. Examination of thermodynamic principles indicates that as the dynamic pressure increases, larger shock waves can be tolerated. The analysis of LASNEX-simulated free-surface velocity profiles using the ILA shows that the method can be used when shock waves are present in the experimental data. This is in part due to the fact that the Rankine-Hugoniot equations and the Taylor expanded Riemann invariants agree to second order in density. However, care must be taken in the analysis to examine the magnitude of the systematic uncertainties associated with the ILA when weak shocks are present. One should ensure that the systematic uncertainties are smaller than the random uncertainties associated with the measurement. Comparison of the stress-density path determined using the ILA and LASNEX tracer particles shows that the peak densities are within 0.7%, less than typical laser-based experimental uncertainties. Systematic offsets due to both shock heating and the use of the ILA results in a stiffer stress-density determination. Experiments with weak shocks analyzed using ILA represent upper bounds to the isentrope that often lie within the experimental uncertainties.

Acknowledgments

It is a pleasure to acknowledge the work of the target fabrication engineer Mr. Walter Nederbracht, Dr. Paul Mirkarimi who manufactured the tantalum parts and Dr. Philip Stern who explained the difference in the EOS tables presented. Without their outstanding contribution this work would not have been possible. This work was performed under the auspices of the U.S. Department of Energy by Lawrence Livermore National Laboratory under Contract DE-AC52-07NA27344.

[1] C. J. Pickard and R. J. Needs, "Dense low-coordination phases of lithium," *Physical Review Letters*, vol. 102, no. 14, p. 146401, 2009.

[2] J. P. Chris and R. J. Needs, "Ab initio random structure searching," *Journal of Physics: Condensed Matter*, vol. 23, no. 5, p. 053201, 2011.

[3] M. Martinez-Canales, C. J. Pickard, and R. J. Needs, "Thermodynamically stable phases of carbon at multiterapascal pressures," *Physical Review Letters*, vol. 108, no. 4, p. 045704, 2012.

[4] E. Wigner and F. Seitz, "On the constitution of metallic sodium," *Physical Review*, vol. 43, no. 10, pp. 804–810, 1933. PR.

[5] B. Rousseau and N. W. Ashcroft, "Interstitial electronic localization," *Physical Review Letters*, vol. 101, no. 4, p. 046407, 2008.

[6] J. R. Rygg, J. H. Eggert, A. E. Lazicki, F. Coppari, J. A. Hawreliak, D. G. Hicks, R. F. Smith, C. M. Sorce, T. M. Uphaus, B. Yaakobi, and G. W. Collins, "Powder diffraction from solids in the terapascal regime," *Review of Scientific Instruments*, vol. 83, no. 11, pp. 113904–7, 2012.

[7] R. F. Smith, J. H. Eggert, R. Jeanloz, T. S. Duffy, D. G. Braun, J. R. Patterson, R. E. Rudd, J. Biener, A. E. Lazicki, A. V. Hamza, J. Wang, T. Braun, L. X. Benedict, P. M. Celliers, and G. W. Collins, "Ramp compression of diamond to five terapascals," *Nature*, vol. 511, no. 7509, pp. 330–333, 2014.

[8] D. Valencia, R. J. O'Connell, and D. Sasselov, "Internal structure of massive terrestrial planets," *Icarus*, vol. 181, no. 2, pp. 545–554, 2006.

[9] D. C. Swift, J. H. Eggert, D. G. Hicks, S. Hamel, K. Caspersen, E. Schwegler, G. W. Collins, N. Nettelmann, and G. J. Ackland, "Mass-radius relationships for exoplanets," *The Astrophysical Journal*, vol. 744, no. 1, p. 59, 2012.

[10] P. J. Tackley, M. Ammann, J. P. Brodholt, D. P. Dobson, and D. Valencia, "Mantle dynamics in super-earths: Post-perovskite rheology and self-regulation of viscosity," *Icarus*, vol. 225, no. 1, pp. 50–61, 2013. Cited By (since 1996):4 Export Date: 3 April 2014 Source: Scopus.

[11] C. A. Haynam, P. J. Wegner, J. M. Auerbach, M. W. Bowers, S. N. Dixit, G. V. Erbert, G. M. Heestand, M. A. Henesian, M. R. Hermann, K. S. Jancaitis, K. R. Manes, C. D. Marshall, N. C. Mehta, J. Menapace, E. Moses, J. R. Murray, M. C. Nostrand, C. D. Orth, R. Patterson, R. A. Sacks, M. J. Shaw, M. Spaeth, S. B. Sutton, W. H. Williams, C. C. Widmayer, R. K. White, S. T. Yang, and B. M. Van Wonterghem, "National ignition facility laser performance status," *Appl. Opt.*, vol. 46, no. 16, pp. 3276–3303, 2007.

[12] J. R. Asay, "Isentropic compression experiments on the Z accelerator," *AIP Conference Proceedings*, vol. 505, no. 1, pp. 261–266, 2000.

[13] J.-P. Davis, "Experimental measurement of the principal isentrope for aluminum 6061-T6 to 240 GPa," *Journal of Applied Physics*, vol. 99, no. 10, pp. –, 2006.

[14] M. D. Knudson, M. P. Desjarlais, and D. H. Dolan, "Shock-wave exploration of the high-pressure phases of carbon," *Science*, vol. 322, no. 5909, pp. 1822–1825, 2008.

[15] D. K. Bradley, J. H. Eggert, R. F. Smith, S. T. Prisbrey, D. G. Hicks, D. G. Braun, J. Biener, A. V. Hamza, R. E. Rudd, and G. W. Collins, "Diamond at 800 GPa," *Physical Review Letters*, vol. 102, no. 7, p. 075503, 2009.

[16] A. L. Kritcher, T. Doppner, D. Swift, J. Hawreliak, G. Collins, J. Nilsen, B. Bachmann, E. Dewald, D. Strozzi, S. Felker, O. L. Landen, O. Jones, C. Thomas, J. Hammer, C. Keane, H. J. Lee, S. H. Glenzer, S. Rothman, D. Chapman, D. Kraus, P. Neumayer, and R. W. Falcone, "Probing matter at Gbar pressures at the NIF," *High Energy Density Physics*, vol. 10, no. 0, pp. 27–34, 2014.

[17] F. Coppari, R. F. Smith, J. H. Eggert, J. Wang, J. R. Rygg, A. Lazicki, J. A. Hawreliak, G. W. Collins, and T. S. Duffy, "Experimental evidence for a phase transition in magnesium oxide at exoplanet pressures," *Nature Geosci*, vol. 6, no. 11, pp. 926–929, 2013.

[18] J. R. Maw, "A characteristics code for analysis of isentropic compression experiments," *AIP Conference Proceedings*, vol. 706, no. 1, pp. 1217–1220, 2004.

[19] S. D. Rothman and J. Maw, "Characteristics analysis of isentropic compression experiments (ice)," *J. Phys. IV France*, vol. 134, pp. 745–750, 2006.

[20] R. F. Smith, J. H. Eggert, D. C. Swift, J. Wang, T. S. Duffy, D. G. Braun, R. E. Rudd, D. B. Reisman, J.-P. Davis, M. D. Knudson, and G. W. Collins, "Time-dependence of the alpha to epsilon phase transformation in iron," *Journal of Applied Physics*, vol. 114, no. 22, pp. –, 2013.

[21] A. H. Jones, W. M. Isbell, and C. J. Maiden, "Measurement of the very-high-pressure properties of materials using a light-gas gun," *Journal of Applied Physics*, vol. 37, no. 9, pp. 3493–3499, 1966.

[22] K. M. Ogilvie and G. E. Duvall, "Shock-induced changes in the electronic spectra of liquid CS_2," *The Journal of Chemical Physics*, vol. 78, no. 3, pp. 1077–1087, 1983.

[23] C. S. Yoo, G. E. Duvall, J. Furrer, and R. Granholm, "Effects of pressure and dilution on the visible and ultraviolet spectrum of

liquid carbon disulfide under shock compression," *The Journal of Physical Chemistry*, vol. 93, no. 8, pp. 3012–3021, 1989.

[24] W. J. Nellis, S. T. Weir, and A. C. Mitchell, "Minimum metallic conductivity of fluid hydrogen at 140 GPa (1.4 Mbar)," *Physical Review B*, vol. 59, no. 5, pp. 3434–3449, 1999. PRB.

[25] W. J. Nellis, "Dynamic compression of materials: metallization of fluid hydrogen at high pressures," *Reports on Progress in Physics*, vol. 69, no. 5, p. 1479, 2006.

[26] Y. Zel'dovich and Y. Raizer, *Physics of Shock Waves and High-temperature Hydrodynamic Phenomena*. DOVER PUBN Incorporated, 2002.

[27] J. Wang, R. F. Smith, J. H. Eggert, D. G. Braun, T. R. Boehly, J. Reed Patterson, P. M. Celliers, R. Jeanloz, G. W. Collins, and T. S. Duffy, "Ramp compression of iron to 273 GPa," *Journal of Applied Physics*, vol. 114, no. 2, pp. 023513–023513–8, 2013.

[28] S. D. Rothman, J. P. Davis, J. Maw, C. M. Robinson, K. Parker, and J. Palmer, "Measurement of the principal isentropes of lead and lead-antimony alloy to $\sim$400 mbar by quasi-isentropic compression," *Journal of Physics D: Applied Physics*, vol. 38, no. 5, p. 733, 2005.

[29] R. Courant and K. Friedrichs, *Supersonic flow and shock waves*. Springer, 1976.

[30] D. Serre, *Systems of Conservation Laws 1: Hyperbolicity, Entropies, Shock Waves*. Cambridge University Press, 1999.

[31] R. L. Kauffman, L. J. Suter, C. B. Darrow, J. D. Kilkenny, H. N. Kornblum, D. S. Montgomery, D. W. Phillion, M. D. Rosen, A. R. Theissen, R. J. Wallace, and F. Ze, "High temperatures in inertial confinement fusion radiation cavities heated with 0.35 μm light," *Physical Review Letters*, vol. 73, no. 17, pp. 2320–2323, 1994.

[32] P. Celliers, "Line-imaging velocimeter for shock diagnostics at the OMEGA laser facility," *Rev. Sci. Instrum.*, vol. 75, no. 11, p. 4916, 2004.

[33] G. B. Zimmerman and W. L. Kruer, "Numerical simulation of laser-initiated fusion," *Comments Plasma Phys. Controlled Fusion*, vol. 2, pp. 51–61, 1975.

[34] D. C. Swift, R. G. Kraus, E. N. Loomis, D. G. Hicks, J. M. McNaney, and R. P. Johnson, "Shock formation and the ideal shape of ramp compression waves," *Physical Review E*, vol. 78, no. 6, p. 066115, 2008. PRE.

[35] C. W. Greeff, "New Sesame equation of state for tantalum," Tech. Rep. LA-13681-MS, Lawrence Livermore National Laboratory, 2000.

[36] R. M. More, K. H. Warren, D. A. Young, and G. B. Zimmerman, "A new quotidian equation of state (QEOS) for hot dense matter," *Physics of Fluids*, vol. 31, no. 10, pp. 3059–3078, 1988.

[37] D. A. Young and E. M. Corey, "A new global equation of state model for hot, dense matter," *Journal of Applied Physics*, vol. 78, no. 6, pp. 3748–3755, 1995.